Interdependence between training and magnetization reversal in granular exchange bias Co-CoO systems

E Menéndez[1,7], T Dias[1,2], J Geshev[2], J F Lopez-Barbera[3], J Nogués[3,4], R Steitz[5], B J Kirby[6], J A Borchers[6], L M C Pereira[1], A Vantomme[1] and K Temst[1]

[1]Instituut voor Kern- en Stralingsfysica, KU Leuven, Celestijnenlaan 200 D, BE-3001 Leuven, Belgium
[2]Instituto de Física, Universidade Federal do Rio Grande do Sul (UFRGS), Porto Alegre, 91501-970 Rio Grande do Sul, Brazil
[3]ICN2-Institut Catala de Nanociencia i Nanotecnologia, Campus UAB, 08193 Bellaterra (Barcelona), Spain
[4]ICREA-Institució Catalana de Recerca i Estudis Avançats, Barcelona, Spain
[5]Helmholtz-Zentrum Berlin für Materialien und Energie GmbH, Hahn-Meitner-Platz 1, 14109 Berlin, Germany
[6]Center for Neutron Research, National Institute of Standards and Technology, Gaithersburg, Maryland 20899, USA

[7]Author to whom any correspondence should be addressed. E-mail: Enric.MenendezDalmau@fys.kuleuven.be

Abstract

The interdependence between training and magnetization reversal in granular exchange bias Co-CoO systems prepared by ion implantation is demonstrated by polarized neutron reflectometry. While high-fluence O-implanted thin films show reduced relative training values and no asymmetry in magnetization reversal (all reversals take place by domain wall nucleation and motion), low-fluence O ion implantation results in an enhanced relative training and a magnetization reversal asymmetry between the first descending and the second ascending virgin branches. Whereas the first untrained reversal occurs mainly by domain wall nucleation and motion, traces of a domain rotation contribution are evidenced in the second untrained reversal. This is partially explained by the evolution of the CoO structure and the contribution of the out-of-plane magnetization with ion implantation. This reveals that the interdependence between training and magnetization reversal is insensitive to the morphology of the constituents (i.e., granular or layered), indicating that this is an intrinsic exchange bias effect, which can be conveniently tailored by the interplay between the intrinsic properties of the investigated materials and ion implantation.

1. Introduction

Exchange bias (EB) [1]–[6] is generally believed to arise from the magnetic exchange coupling between a ferromagnet (FM) and the uncompensated interfacial antiferromagnetic spins of an adjacent antiferromagnet (AFM), which are pinned by the AFM and do not follow

the applied magnetic field ($H_{applied}$) [7]–[9], although more complex scienarions (e.g., uncompensated spins in the FM or uncompensated spins in the bulk of the AFM) have been proposed [10,11]. This interfacial phenomenon is typically set by field cooling the system below the Néel temperature of the AFM, resulting usually in a shift along the field axis (H_E) and a broadening of the hysteresis loop of the FM (H_C enhancement) [3]–[6]. Frequently, when magnetically cycling the system, the EB shift decreases monotonically down to a steady value, $H_E^{n=\infty}$ (where n labels the number of consecutively measured hysteresis loops). That is, a fraction of pinned interfacial spins becomes gradually reversible with $H_{applied}$ upon cycling the system and, therefore, do not contribute further to H_E [3]–[6], [12]–[16]. The dependence of H_E on n reveals the so-called training effect, an ageing-like phenomenon which is related to the metastable state of the AFM and/or the FM/AFM interface upon field cooling. Training is a consequence of changes in the spin structure which evolves from a non-equilibrium toward an equilibrium configuration, indicating that the reversal of formerly anchored spins occurs partly and progressively over an energy barrier distribution [12, 13]. Often, thermal and athermal training are discerned depending on the presence or absence of thermally-assisted effects. While the athermal training is virtually temperature independent and characterized by an abrupt suppression of H_C and H_E between the first and the second consecutively measured hysteresis loops, the thermal training vanishes at low temperature and usually brings about small changes in both H_E and H_C during each loop trace for $n > 2$ [14, 16]. Athermal training effects may occur due to spin-flop-like FM/AFM coupling in systems with highly symmetric AFMs (i.e., with multiple AFM easy anisotropy axes) [18, 19]. However, it has been recently demonstrated that, in the framework of granular-like FM/AFM interfaces, athermal training can also arise due to exchange and/or dipolar interactions between neighboring interfacial spin clusters regardless of the anisotropy type of the AFM [12], suggesting that interfacial

morphology may result in an additional training on top of that already known to arise from the AFM magnetic symmetry.

Another intriguing feature of EB systems is the magnetization reversal asymmetry (i.e., different mechanisms for magnetization reversal on field-decreasing and field-increasing branches of the untrained hysteresis loop), which has been commonly observed in exchange bias AFM/FM bilayers and investigated by a number of experimental techniques [20]–[26]. Even though the mechanisms appear to differ among systems, the origin of the asymmetric reversal has been often correlated with the existence of higher order FM anisotropies [20, 21], local misalignments of the easy magnetization axes of the FM and AFM [20], irreversibilities due to training [22, 23], or a competition between anisotropies in th3 framework of either the fixed interface AFM moments model [25] or the AFM domain-wall formation one [26]. Although the correlation between training and reversal asymmetry in EB systems still remains intricate not only from its physical origin but also from its lack of control, evidences of the interdependence between training and magnetization reversal in layered FM/AFM systems have been recently revealed [27, 28]. Notably, this correlation has only been proven for bilayered systems and conformation on other types of morphologies to establish the universality of this effect, is still lacking. However, it is worth insisting on the complexity of the interplay between training and magnetization reversal since the transient dynamics of magnetic moments (i.e., pathways to equilibrium) can largely influence the final local energy minimum the system reaches [29, 30].

In the last decades, EB has gained technological importance since it is used to establish a reference direction in *spintronic* devices, such as magnetic read heads of hard disk drives [31, 32]. Since exchange bias thin films play an essential role in *spintronics*, the vast majority of EB research has been mostly focused on thin films, where Co and CoO have turned out to be the

archetypal FM and AFM, respectively [1]–[6], constituting a valuable model system [33]. Typically, the formation of AFM CoO in thin films relies on surface oxidation by exposing the sample to air or to a controlled oxygen atmosphere (i.e., bilayer). Since surface oxidation is a self-limiting process, it results in an oxide thickness of only a few nanometers, which forms a single interface between Co and CoO. Nevertheless, ion implantation has been demonstrated as a suitable procedure to control the amount of AFM and, ultimately, the EB properties of FM-AFM systems, such as Co-CoO [34]–[36] or Ni-NiO [37], by forming multiple FM-AFM interfaces (i.e., granular-like) controllably distributed throughout the FM matrix.

In this article, the interdependence between training and magnetization reversal is demonstrated by magnetic field scans in polarized neutron reflectometry, in granular exchange bias Co-CoO systems prepared by ion implantation. Moreover, the results show that training and magnetization reversal can be conveniently controlled by the interplay between the intrinsic properties of the studied materials and ion implantation.

2. Experimental

Polycrystalline 30 nm thick Co thin films were grown by molecular beam epitaxy on thermally-oxidized Si (100) substrates which were previously covered with a 10 nm thick Au buffer layer. Then, either a 15 nm or 30 nm thick Au capping layer was deposited in order to protect the Co from surface oxidation. All layers were grown at room temperature at a pressure of around 3×10^{-10} mbar. The films with a 15 nm thick Au capping layer were then implanted using O ions, with energy of 40 keV, at fluences of 3×10^{16}, 5×10^{16}, 1×10^{17}, 1.2×10^{17}, 1.5×10^{17} and 2×10^{17} ions/cm^2. With the aim to produce larger amounts of CoO, samples with a 30 nm thick Au capping layer were implanted at 3.25×10^{17} and 5.5×10^{17} ions/cm^2 using an energy of 50 keV. As shown in previously reported studies on this type of system, the implantation gives rise to a rather uniform implantation profile of O [33] with an atomic O concentration at half depth of

the Co layer of around 5, 8, 15, 18, 21, 26, 34 and 44% for the films implanted at 3×10^{16}, 5×10^{16}, 1×10^{17}, 1.2×10^{17}, 1.5×10^{17}, 2×10^{17}, 3.25×10^{17} and 5.5×10^{17} ions/cm^2, respectively.

The samples were structurally characterized by transmission electron microscopy (TEM) and synchrotron grazing incidence X-ray diffraction (GIXRD) at an angle of 1.5 degrees using a wavelength of 1.199 Å. The GIXRD measurements were performed at the Rossendorf (Helmholtz Zentrum Dresden-Rossendorf) BM20 beamline at the European Synchrotron Radiation Facility (ESRF).

Superconducting quantum interference device (SQUID) magnetometry was used to study the exchange bias properties at 10 K after being induced by field cooling the samples from room temperature in an in-plane applied magnetic field of 400 mT. Training effects were studied by magnetically cycling the system (i.e., by tracing consecutive SQUID hysteresis loops) until equilibrium (i.e., saturation of the exchange bias shift, H_E^{∞}) was reached.

Polarized neutron reflectometry (PNR) was used to unravel the magnetization reversal mechanisms at 10 K after the field cooling procedure described above. From the polarized reflectivity pattern recorded in the saturated magnetization state, the angle (i.e., the incidence angle of neutrons) showing a good tradeoff between intensity and splitting ratio was selected to perform magnetic field scans (i.e., at a certain angle, the non-spin flip (NSF) and the spin flip (SF) signals are recorded as a function of $H_{applied}$). The NSF reflectivity originates from the neutron interaction with the sample nuclei and the interaction of the neutron spin with the in-plane magnetization component parallel to $H_{applied}$. Conversely, the SF reflectivity results from the interaction of the neutron spin with the in-plane magnetization component perpendicular to the external magnetic field [38]–[40]. Upon reflection, the neutron polarization is analyzed, resulting in four different measured reflectivities: two NSF signals, uu and dd, and two SF signals, ud and du. The first index denotes the polarization prior to reflection and the second index the polarization after reflection. The measurements were performed at the V6-

reflectometer [41] of the Helmholtz-Zentrum für Materialien und Energie (Berlin). This reflectometer uses a neutron wavelength of 4.66 Å. To polarize the beam and to analyze the neutron polarization after reflection, polarizing Si/FeCo supermirrors are used. Detection of the reflected neutrons is carried out by ^{3}He tubes. In order to maintain the polarization of the neutrons throughout the reflectometer, guide fields are mounted at dedicated positions. Since neutrons depolarize due to stray fields when a negative $H_{applied}$ is applied, the measurements can only be performed at positive fields. Hence, in order to assess the descending branches (which usually lie at negative fields after cooling in a positive field), the samples are cooled in a negative field, implying that the aforementioned descending branches will then reside at positive fields. The ascending and descending branches were in fact measured after separate field cooling processes which explains why the magnetic field scans always have a positive magnetic field scale.

3. Results

As can be seen in Figures 1a and 1b, the as-deposited SiO_2 / 10 nm Au / 30 nm Co / 15 nm Au sample shows well-defined Au/Co interfaces, whereas the implantation leads to an increased roughness between layers. The implantation also yields Co-Au and Co-Si/Co-O intermixtures which extend up to around some nanometers [36]. High-angle annular dark-field imaging in scanning TEM mode (not shown) was used to map the Au, Co and O distributions along the cross-section of the samples, evidencing that the main role of the implanted oxygen is to further oxidize the grain boundaries in Au, leading to O-free Au grains surrounded by an O-rich Au phase. Concerning the Co layer, due to the rapid oxidation of Co when exposed to air no conclusions can be drawn from the TEM analysis. However, a process similar to the one observed for Au is expected. Synchrotron GIXRD reveals that the Co layer of the as-deposited sample (not shown) consists of a mixture of face-centered cubic (FCC) Co and hexagonal close-

packed (HCP) Co, in agreement with previously reported results [36]. The amount of CoO phase increases with implantation fluence (Figure 1c), as evidenced by the increase of intensity of the CoO XRD peaks in detriment of the Co and Au lines. This is in agreement with the growth of the CoO counterpart with implantation fluence. After implanting at 5.5×10^{17} ions/cm^2, virtually no traces of metallic Co are observed. Furthermore, the signal-to-noise ratio of the GIXRD patterns worsens with implantation fluence, evidencing that the amount of crystalline metallic Co decreases because of the increased density of induced defects, such as stacking faults, grain boundaries or interfaces with the Au buffer and the capping layer, and the CoO formation.

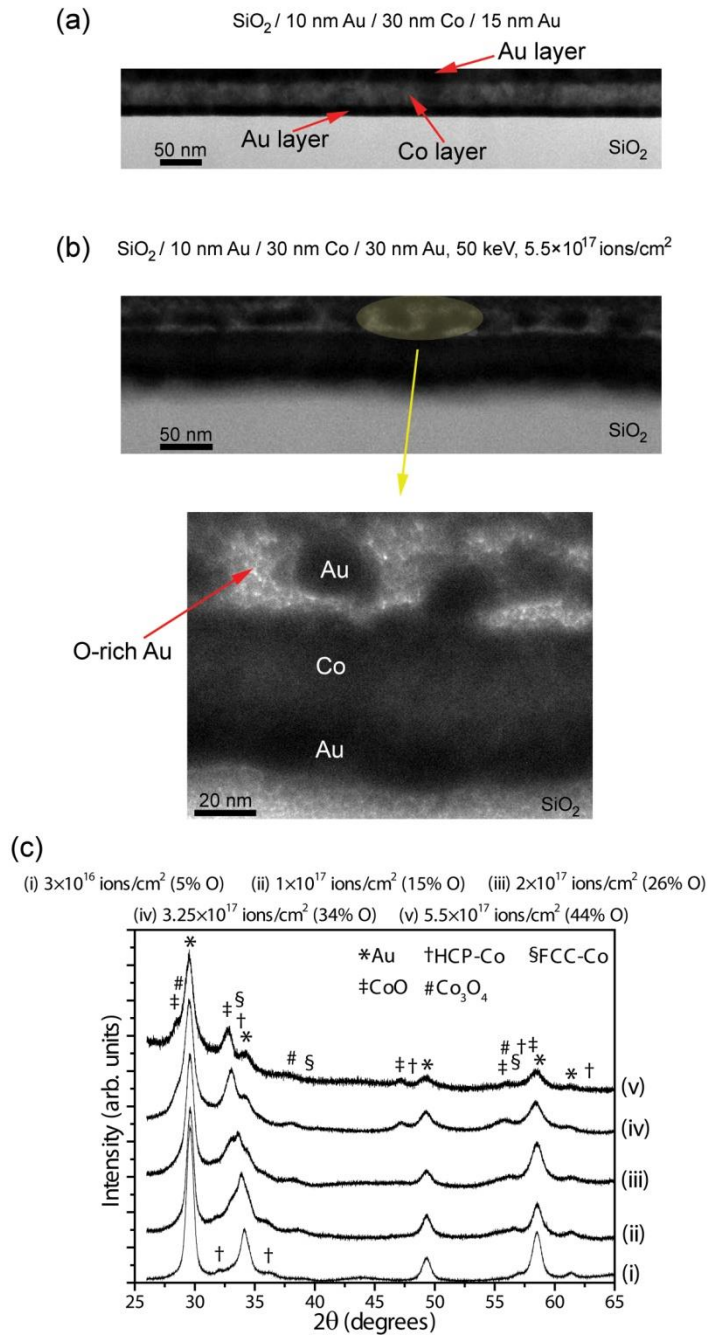

Figure 1. (a) Transmission electron microscopy (TEM) image of the cross-section of the as-deposited sample, (b) cross-sectional TEM image of the film implanted with 50 keV O ions at 5.5×10^{17} ions/cm^2 and (c) synchrotron grazing incidence X-ray diffraction patterns corresponding to the samples implanted with 40 keV O ions, at 3×10^{16} (5% O), 1×10^{17} (15% O) and 2×10^{17} ions/cm^2 (26% O), and with 50 keV O ions, at 3.25×10^{17} ions/cm^2 (34% O) and 5.5×10^{17} ions/cm^2 (44% O). The peaks of Au (64701-ICSD –Inorganic Crystal Structure Database–), HCP-Co (76633-ICSD), CoO (9865-ICSD) and FCC-Co (76632-ICSD) are indicated in the figure [40]. Since weak traces of Co_3O_4 (28158-ICSD) are observed, only the main peaks of Co_3O_4 are labeled.

Figure 2 shows the consecutive SQUID measurements at 10 K corresponding to the films implanted at 3×10^{16} (5% O), 1.2×10^{17} (18% O), 2×10^{17} (26% O) and 5.5×10^{17} ions/cm^2 (44%

O), respectively. The 5% O sample needs only 3 consecutive hysteresis loops to level off the exchange bias shift (Figure 2a), whereas the 26% O and 44% O samples require 8 cycles (Figures 2c and 2d, respectively). That is, the training stabilization delays with increasing implantation fluence until reaching, to some extent, saturation (see Figure 2e, which displays the training behavior, expressed as $-\mu_0(H_E^n - H_E^{10})$ vs. n).

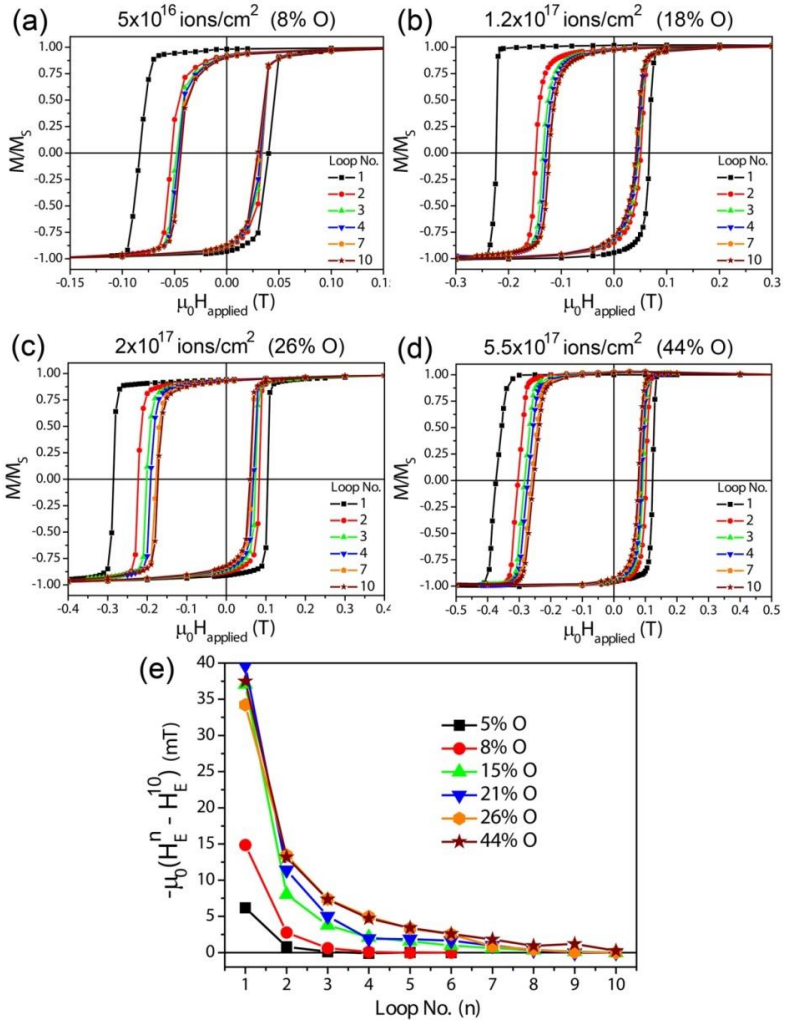

Figure 2. (a), (b), (c) and (d) are the consecutive SQUID measurements at 10 K corresponding to the films implanted at 3×10^{16} (5% O), 1.2×10^{17} (18% O), 2×10^{17} (26% O) and 5.5×10^{17} ions/cm^2 (44% O), respectively. (e) Training behavior, expressed as $-\mu_0(H_E^n - H_E^{10})$. The lines are guides to the eye.

This postponement of training with implantation can be quantified under the framework of Binek's model [12, 13]. In this context, if $|H_E^\infty|$ is taken from the experimental results, the γ parameter, which is related to the free energy of the system, can be quantified as $\gamma_N =$

$\frac{1}{N-1}\sum_{n=1}^{N-1}\frac{(|H_E^n|-|H_E^{n+1}|)}{(|H_E^n|-|H_E^\infty|)^3}\gamma_N = \frac{1}{N\text{-}1}\sum_{n=1}^{N\text{-}1}\frac{(|H_E^n|\text{-}|H_E^{n+1}|)}{(|H_E^n|\text{-}|H_E^\infty|)}$, where N stands for the last loop taken into account in the calculation. A large value of γ requires a small absolute training (i.e., small deviations from equilibrium) and a large value of $|H_E^n| - |H_E^{n+1}|$. This implies that training exhibits an abrupt behavior (i.e., the reduction of H_E primarily takes place between the first and the second measured hysteresis loops), which is often quantified by the steepness of the H_E vs. n curves: $\frac{|H_E^1|-|H_E^2|}{|H_E^1|-|H_E^\infty|} \times 100$ (%). Conversely, a small value of γ involves a large absolute training and a small value of $|H_E^n| - |H_E^{n+1}|$, leading to a gradual degradation of H_E, which is spread over a larger number of cycles. As can be seen in Figure 2e, the γ parameter has been quantified after taking into account three loops (i.e., γ_3). γ_3 decreases with increasing fluence until reaching a steady state. Around 20 at. % of incorporated O, a transition-like behavior of the evolution of γ_3 with the amount of O is observed (Figure 3). Above 20 at. % of O (i.e., low values of γ_3), the absolute training strength (i.e., $|H_E^1| - |H_E^\infty|$) is spread over a larger number of cycles, indicating that training occurs more gradually. Accordingly, the samples exhibiting larger γ_3 values (i.e., samples with O contents below 20 at. % of O) are those which show more steepness and, therefore, a faster stabilization of training with n. Moreover, as can be also seen in Figure 3, both the steepness and the relative training decrease with implantation fluence.

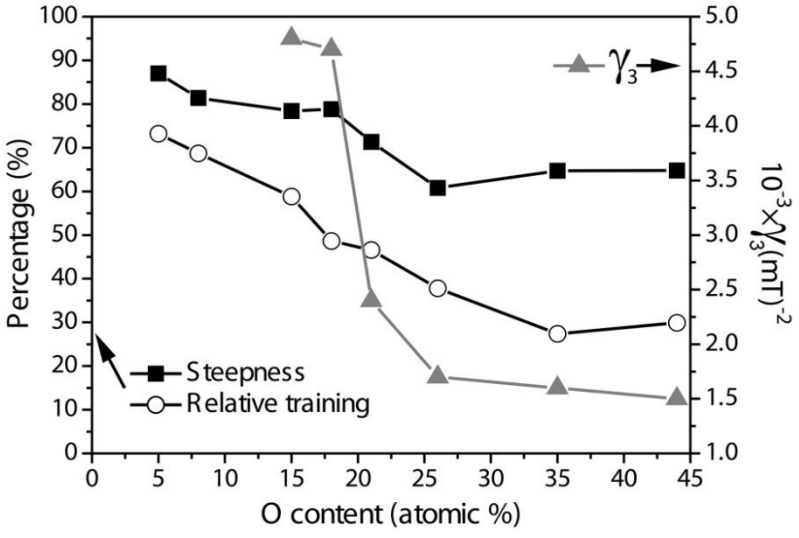

Figure 3. Dependence of the γ parameter quantified after taking into account three consecutive loops (i.e., γ_3), the steepness ($\frac{|H_E^1|-|H_E^2|}{|H_E^1|-|H_E^\infty|} \times 100$ (%)) and the relative training ($\frac{|H_E^1|}{|H_E^1|-|H_E^\infty|} \times 100$ (%)) on the content of incorporated O. Note that $|H_E^\infty|$ was taken as $|H_E^6|$ for the samples implanted at 3×10^{16} and 5×10^{16} ions/cm^2 and as $|H_E^{10}|$ for the rest of samples. The γ_3 parameter is not presented for the samples implanted at 3×10^{16} and 5×10^{16} ions/cm^2 since the training almost fully stabilizes after the second measured loop. The lines are guides to the eye.

Magnetic field scans in specular PNR have been used to unravel the in-plane magnetization reversal mechanism of two representative samples, i.e., one implanted above and another one below the O content threshold which determines the transition in γ_3. Namely, a sample exhibiting a rather steep behavior with increased relative training and another one showing a more gradual training and decreased relative training were studied. Figure 4 shows the magnetic field scans at 10 K of the untrained loop (virgin, a and d), the first trained loop (second loop in total, b and e) and the seventh trained loop (eight loop in total, c and f) corresponding to the sample implanted at 5.5×10^{17} ions/cm^2. In all reversals, the NSF signals (uu and dd) cross halfway between the minimum and maximum values of the NSF signals, indicating that the total NSF intensity remains constant and, thus, the probed magnetization remains with reversals in the plane of the sample. In concordance, the spin flip intensities hardly increase above the background level, implying the absence of any perpendicular magnetization component during the reversal. Consequently, all reversals occur via domain wall nucleation and motion.

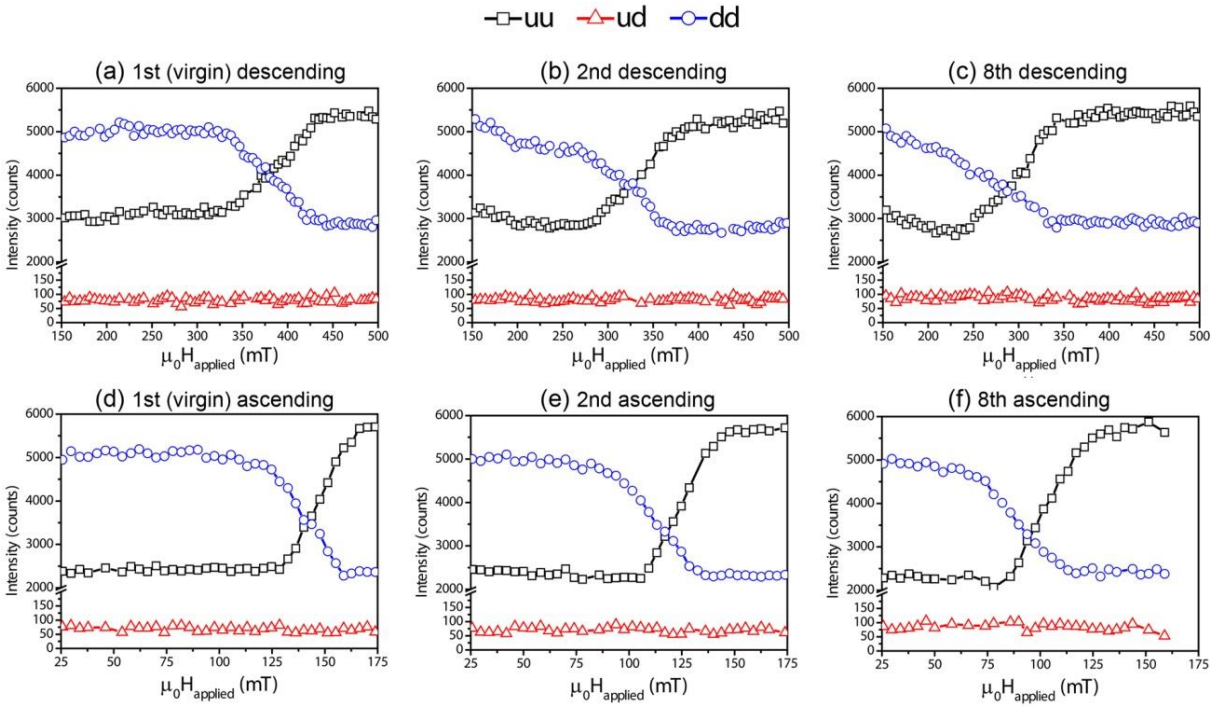

Figure 4. (a), (b), (c), (d), (e) and (f) are the magnetic field scans in polarized neutron reflectometry at 10 K and after field cooling in an in-plane applied magnetic field of 400 mT corresponding to the 1st descending, 2nd descending, 8th descending, 1st ascending, 2nd ascending and 8th ascending branches of the film implanted with 50 keV O ions at 5.5×10^{17} ions/cm^2 (44% O). The lines are guides to the eye. Since ud and du are analogous signals, only the ud spin flip signal has been plotted.

Conversely, the sample implanted at 1.2×10^{17} ions/cm^2 exhibits a clear asymmetry in magnetization reversal between the first (virgin descending) and the second (virgin ascending) magnetization inversions (Figure 5). While the crossing of the NSF intensities of the 1st descending branch lies slightly below the middle between the minimum and maximum NSF intensities, the crossing of the rest of reversals takes place at the bottom of the NSF intensities. In parallel, the SF intensity slightly increases with reversals, suggesting that the contribution of a perpendicular magnetization component reinforces while consecutively switching the magnetization (i.e., enhanced domain rotation mechanism). It should be pointed out that Zeeman splitting might be to some extent ruled out as the source of this SF signal since transversal SQUID measurements (not shown) confirm the presence of an in-plane transversal (i.e., perpendicular to the

applied magnetic field) component in the sample implanted at 1.2×10^{17} ions/cm^2 while this is virtually negligible for the sample implanted at 5.5×10^{17} ions/cm^2.

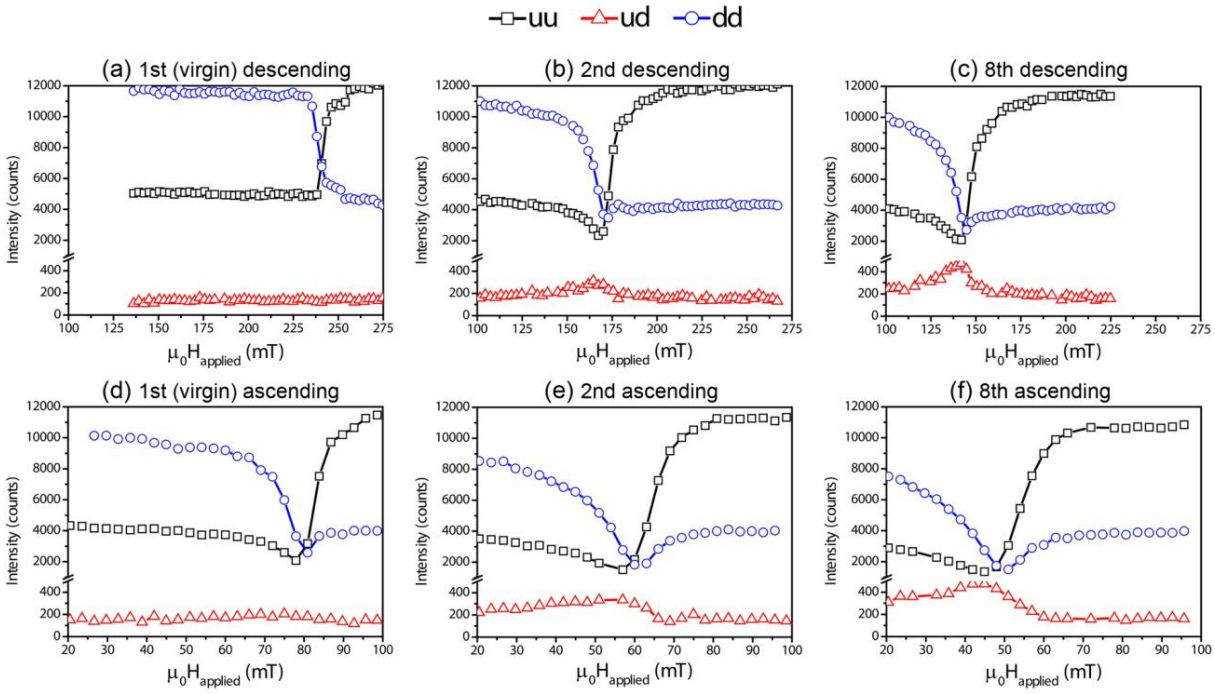

Figure 5. (a), (b), (c), (d), (e) and (f) are the magnetic field scans in polarized neutron reflectometry at 10 K and after field cooling in an in-plane applied magnetic field of 400 mT corresponding to the 1st descending, 2nd descending, 8th descending, 1st ascending, 2nd ascending and 8th ascending branches of the film implanted with 40 keV O ions at 1.2×10^{17} ions/cm^2 (18% O). The lines are guides to the eye. Since ud and du are analogous signals, only the ud spin flip signal has been plotted.

Figure 6 shows the evolution with the measured magnetization reversal of the difference between the uu and ud signals (normalized to the uu intensity) at the crossing between the NSF signals. The relative intensity between NSF and SF signals remains rather unaltered in the sample implanted at 5.5×10^{17} ions/cm^2, suggesting that reversals of the probed magnetization occur in the plane of the sample. In contrast, for the sample implanted at 1.2×10^{17} ions/cm^2, the relative intensity significantly decreases with the magnetization reversals, evidencing a progressive loss of intensity which might be linked to off-specular scattering, which cannot be fully detected by specular PNR, and/or out-of-plane contributions, which PNR is not sensitive to.

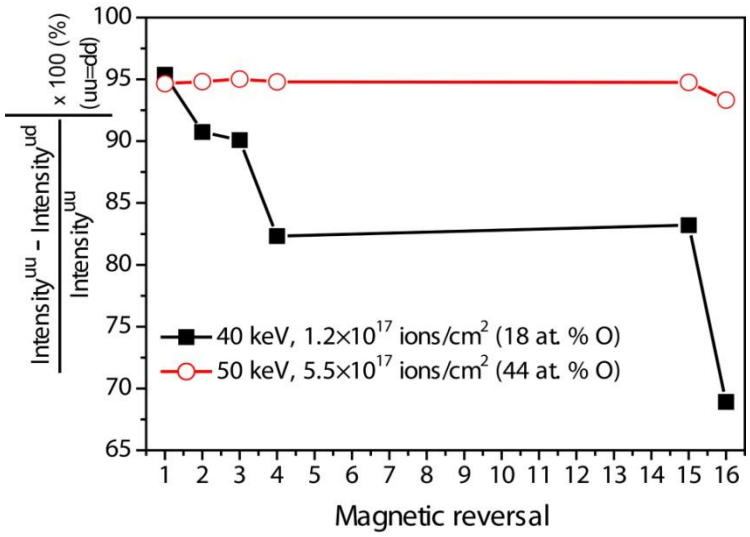

Figure 6. Evolution with the measured magnetization reversal of the difference between the uu and ud signals (normalized to the uu intensity) at the crossing between the NSF signals. The lines are guides to the eye.

4. Discussion

Cross-sectional TEM results evidence that O ion implantation into capped Co thin films induces a pronounced atomic intermixing and roughness between layers (Figure 1). As can be seen in Figure 1b, the main role of the incorporated oxygen is to further oxidize the grain boundaries in Au, leading to O-free Au grains surrounded by a O-rich Au phase, in analogy with the already reported grain boundary oxidation mechanism responsible for the O incorporation in O-implanted Co thin films [35, 36]. Since the TEM sample preparation involves the exposition of the sample to air and metallic Co is highly reactive to O (forming Co oxides) while Au is virtually non-reactive, the grain boundary oxidation mechanism is only distinguished by TEM in the Au phase. Nevertheless, the amount of CoO increases with implantation fluence as evidenced by synchrotron GIXRD (Figure 1c), resulting in thicker CoO grain boundaries with improved stoichiometry, which are less prone to size effects (i.e., less nanostructured) [36].

As can be seen in Figure 2, in contrast to O-implanted thin films with Gaussian-like O depth profiles which display inhomogeneous hysteresis loops [34, 36, 37], the loops are rather symmetric and characterized by sharp descending and ascending branches, indicating that

magnetization inversion takes place at well-defined switching fields thus confirming the homogeneity of the O induced profile. Interestingly, as shown in Figure 2e, the stabilization of training slows down (i.e., the steady state of H_E is reached after a larger n) with increasing implantation fluence until reach to some extent saturation. The partial and progressive diminution of the fraction of pinned AFM interfacial spins with n takes place over an energy barrier distribution [14, 44], indicating that the anchored AFM interfacial spins show different degrees of stability (i.e., some are more prone to become loosely coupled and, hence, reverse with the applied magnetic field without further contributing to EB). Thus, since the implantation brings about a broadening of the distribution of structural features, this training postponement might be to some extent ascribed to the widening with ion implantation of the energy barrier distribution to reverse the pinned interfacial spins which eventually causes training to evolve more gradually, extending over a larger number of cycles. This can be satisfactorily quantified under the framework of Binek's model [12, 13]. As can be seen in Figure 3, a transition-like behavior of the evolution of γ_3 with the amount of incorporated O is observed around 20 at. % of O. Below this threshold, samples show an increased relative training and enhanced γ_3 values, evidencing a sharp evolution of training with high steepness values. Conversely, above this threshold, films exhibit decreased relative training values and the training effect spreads over a larger number of cycles, indicating that it takes place more gradually in agreement with the broadening of the distribution of structural features that implantation creates. A similar dichotomy has been already found in Co/CoO systems with thin and thick CoO layers, where thin CoO layers result in large training effects, while training is found to decrease with increasing CoO thickness. Moreover, it has also been reported that, whereas the magnetocrystalline anisotropy in thin (thick) CoO is small (large), the rotatable anisotropy is large (small) [44, 45]. In this context, the implantation yields thicker CoO grain boundaries with

improved stoichiometry, less size effects and increased magnetocrystalline anisotropy in agreement with previously reported results.

The comparison between the magnetic field scans in specular PNR of the film implanted at 5.5×10^{17} ions/cm^2 (Figure 4) and those of the sample implanted at 1.2×10^{17} ions/cm^2 (Figure 5) shows that, while the magnetization reversals of the sample with high CoO content are governed by domain wall nucleation and motion, the sample implanted with lower CoO content exhibits a magnetization reversal asymmetry between the first (virgin descending) and the second (virgin ascending) magnetization reversals. The first reversal is mainly ruled by domain wall nucleation and motion, whereas the second and further reversals show a perpendicular magnetization component which reinforces upon cycling, indicating an increased contribution via rotation of the magnetization. This also clearly evidences the metastable nature of the system after field cooling, which progressively evolves with consecutively measured loops to a local equilibrium state. In contrast to O-implanted Co films with a Gaussian-like O depth profile which exhibit both unbiased Co and a variation of EB strength along film depth and no reversal asymmetry [34, 37], the behavior of the low-fluence implanted samples seems to somewhat recover the asymmetry found in Co/CoO bilayers, where the first reversal mechanism is governed by domain wall nucleation and motion and the rest occur by coherent rotation [21, 22, 46]. In analogy to Co/CoO bilayers [43, 44], the results could be understood in the framework of the level of magnetocrystalline anisotropy achieved with ion implantation. That is, low fluence implantation leads to a CoO phase which is highly prone to scaling effects, far from being stoichiometric and with reduced magnetocrystalline anisotropy, enabling other magnetic easy axes which ultimately are the ones responsible of the magnetization reversal asymmetry and the increased relative training values [27, 28, 44, 45].

As can be seen in Figure 6, the difference, with the measured magnetization reversal, between the uu and ud signals (normalized to the uu intensity) at the crossing between the non

spin flip signals remains rather unaltered in the sample implanted at 5.5×10^{17} ions/cm^2, indicating that reversals take place in the plane of the sample. Conversely, for the sample implanted at 1.2×10^{17} ions/cm^2, a significant loss of intensity with the magnetization reversal is found. Since no traces of off-specular signal are encountered during the magnetic field scans in the background detectors which account to some extent for the off-specular scattering, the formation and evolution of in-plane interfacial magnetic domains might be ruled out as the origin of this loss of intensity [46]. In fact, since PNR is not sensitive to out-of-plane components of the magnetization, this partial loss may be linked to a complex magnetization reversal which evolves with reversals and involves perpendicular (i.e., not fully in-plane) components, indicating that the intrinsic out-of-plane anisotropy of the ferromagnetic counterpart, together with the already mentioned magnetocrystalline anisotropy of the formed CoO, also plays a central role in determining training and magnetization reversal asymmetry in the exchange bias state. This is in agreement with the already reported crucial role of the out-of-plane anisotropy in the occurrence of training [30]. Vector magnetometry at room temperature (not shown) of the sample implanted at 1.2×10^{17} ions/cm^2 confirms the presence of a strong out-of-plane contribution which, as mentioned, might be responsible for the complex evolution of the magnetization with magnetization inversions. More specifically, while the top surface shows perpendicular magnetic anisotropy, the magnetization tends to lie down in-plane in the rest of the sample.

5. Conclusions

The interdependence between training and magnetization reversal in granular exchange bias Co-CoO systems prepared by ion implantation is demonstrated by magnetic field scans in polarized neutron reflectometry. While low-fluence implanted Co thin films exhibit large values of relative training and an asymmetry between the first and the second magnetization reversal,

high-fluence implanted Co thin films show reduced relative training values and no asymmetry in magnetization reversal mechanism. The amount of incorporated O, which determines the threshold of both behaviors, is around 20 at. %. While, at large fluences, the formed CoO grain boundaries are thick and rather stoichiometric with an increased magnetic anisotropy, low-fluence implantation leads to the formation of thin CoO with a less well-defined stoichiometry, highly affected by scaling effects. This results in a decreased CoO magnetic anisotropy, enabling other magnetic easy axes which are partly responsible for the magnetization reversal asymmetry and the increased relative training values. Remarkably, the completion of the explanation comprises the pronounced out-of-plane contribution of the samples implanted at low-fluence O (i.e., below 1.5×10^{17} ions/cm^2), suggesting that the intrinsic out-of-plane anisotropy of the ferromagnetic counterpart plays a significant role in determining training, in agreement with previous reported results [30], and magnetization reversal asymmetry in the exchange biased state. Moreover, the non-equilibrium nature of training evolution with n is clearly observable in the PNR assessment of the low fluence sample implanted sample, where the metastable state reached after field cooling, forced to some extent to keep the magnetization in-plane, progressively evolves to a final local equilibrium state where the overall magnetization of the system exhibits a pronounced out-of-plane contribution. However, since this might involve complex and alternative reversal pathways with perpendicular contributions, the quantitative aspects, such as atomic mechanisms, of the evolution of magnetization reversal in these low-fluence implanted samples is the subject of future studies.

This study shows that both training and magnetization reversal can be tailored by the interplay between the intrinsic properties of the employed materials and ion implantation, underlining that their interdependence is rather insensitive to the morphology of the constituents (i.e., granular or layered), indicating that it is an intrinsic exchange bias effect. This also

demonstrates the great potential of ion implantation to tune the magnetic properties by controllably modifying the local microstructure.

Acknowledgements

This work was financed by the Research Foundation - Flanders (FWO), the Belgian Interuniversity Attraction Poles (IAP P6/42) research programs, the KU Leuven BOF (CREA/07/005) and Concerted Action (GOA/09/006) programs, the 2009-SGR-1292 project of the Generalitat de Catalunya, the MAT2010-20616-C02 project of the Spanish Ministerio de Economía y Competitividad and the European Commission under the 7th Framework Programme through the "Research Infrastructure" action of the "Capacities" Programme, NMI3-II Grant number 283883. We thank HZB (proposal PHY-04-2130) and ESRF (proposal HC-1012, BM20 beamline) for the allocation of neutron and synchrotron radiation beamtime, respectively, and C. Bähtz for the assistance during the synchrotron measurements. E. M. and L.M.C. P. also thank the Fund for Scientific Research - Flanders (FWO) for financial support. T. D. thanks the CNPq agency (project 245897/2012-7) for financial support.

References

[1] Meiklejohn W H and Bean C P 1956 *Phys. Rev.* **102** 1413

[2] Meiklejohn W H and Bean C P 1957 *Phys. Rev.* **105** 904

[3] Nogués J and Schuller I K 1999 *J. Magn. Magn. Mater.* **192** 203

[4] Berkowitz A E and Takano K 1999 *J. Magn. Magn. Mater*. **200** 552

[5] Nogués J, Sort J, Langlais V, Skumryev V, Suriñach S, Muñoz J S and Baró M D 2005 *Phys. Rep.* **422** 65

[6] Radu F and Zabel H *Exchange Bias Effect of Ferro-/Antiferromagnetic Heterostructures* 2007 *Springer Tracts Mod. Phys.* **227** 97

[7] Ohldag H, Scholl A, Nolting F, Arenholz E, Maat S, Young A T, Carey M and Stöhr J 2003 *Phys. Rev. Lett.* **91** 017203

[8] Brück S, Schütz G, Goering E, Ji X S and Krishnan K M 2008 *Phys. Rev. Lett.* **101** 126402

[9] Geshev J, Dias T, Nicolodi S, Cichelero R, Harres A, Acuña J J S, Pereira L G, Schmidt J E, Deranlot C and Petroff F 2011 *J. Phys. D: Appl. Phys.* **44** 095002

[10] Nogués J, Stepanow S, Bollero A, Sort J, Dieny B, Nolting F, Gambardella F 2009 *Appl. Phys. Lett.* **95**, 152515.

[11] Fitzsimmons M R, Kirby B J, Roy S, Li Z P, Roshchin I V, Sinha S K, Schuller I K 2007 *Phys. Rev. B* **75**, 214412.

[12] 6Binek Ch 2004 *Phys. Rev. B* **70** 014421

[13] Binek Ch *Tunable Exchange Bias Effects* 2009 Liu J P, Fullerton E, Gutfleisch O, Sellmyer D J (ed) *Nanoscale Magnetic Materials and Applications* (Springer: New York, USA, first edition)

[14] Harres A and Geshev J 2011 *J. Phys.: Condens. Matter* **23** 216003

[15] Fernandez-Outon L E, Vallejo-Fernandez G, Manzoor S and O'Grady K 2006 *J. Magn. Magn. Mater.* **303** 296

[16] Biternas A G, Nowak U and Chantrell R W 2009 *Phys. Rev. B* **80** 134419

[17] Ali S R, Ghadimi M R, Fecioru-Morariu M, Beschoten B and Güntherodt G 2012 *Phys. Rev. B* **85** 012404

[18] Hoffmann A 2004 *Phys. Rev. Lett.* **93** 097203

[19] Brems S, Temst K and Van Haesendonck C 2007 *Phys. Rev. B* **99** 067201

[20] McCord J, Schäfer R, Mattheis R and Barholz K-U 2003 *J. Appl. Phys.* **93** 5491

[21] Fitzsimmons M R, Yashar P, Leighton C, Schuller I K, Nogués J, Majkrzak C F and Dura J A 2000 *Phys. Rev. Lett.* **84** 3986

[22] Radu F, Etzkorn M, Schmitte T, Siebrecht R, Schreyer A, Westerholt K and Zabel H 2002 *J. Magn. Magn. Mater.* **240** 251

[23] Gierlings M, Prandolini M J, Fritzsche H, Gruyters M and Riegel D 2002 *Phys. Rev. B* **65** 092407

[24] Leighton C, Fitzsimmons M R, Yashar P, Hoffmann A, Nogués J, Dura J, Majkrzak C F and Schuller I K 2001 *Phys. Rev. Lett.* **86** 4394

[25] Jiménez E, Camarero J, Sort J, Nogués J, Mikuszeit N, García-Martín J M, Hoffmann A, Dieny B and Miranda R 2009 *Phys. Rev. B* **80** 014415

[26] Geshev J 2000 *Phys. Rev. B* **62** 5627

[27] Fulara H, Chaudhary S and Kashyap S C 2012 *Appl. Phys. Lett.* **101** 142408

[28] Lund M S and Leighton C 2007 *Phys. Rev. B* **76** 104433

[29] Dieny B and Gavigan J P 1990 *J. Phys.: Condens. Matter* **2** 187

[30] Biagioni P, Montano A and Finazzi M 2009 *Phys. Rev. B* **80** 134401

[31] Dieny B, Speriosu V S, Parkin S S P, Gurney B A, Wilhoit D R and Mauri D 1991 *Phys. Rev. B* **43** 1297

[32] Moser A, Takano K, Margulies D T, Albrecht M, Sonobe Y, Ikeda Y, Sun S and Fullerton E E 2002 *J. Phys. D: Appl. Phys.* **35** R157

[33] Gruyters M and Riegel D 2001 *Phys. Rev. B* **63** 052401

[34] Demeter J, Meersschaut J, Almeida F, Brems S, Van Haesendonck C, Teichert A, Steitz R, Temst K and Vantomme A 2010 *Appl. Phys. Lett.* **96** 132503

[35] Demeter J, Menéndez E, Temst K and Vantomme A 2011 *J. Appl. Phys.* **110** 123902

[36] Menéndez E, Demeter J, Van Eyken J, Jedryka E, Wójcik M, Nawrocki P, Lopez-Barbera J F, Nogués J, Vantomme A and Temst K 2013 *ACS Appl. Mater. Interfaces* **5** 10118

[37] Demeter J, Menéndez E, Schrauwen A, Teichert A, Steitz R, Vandezande S, Wildes A R, Vandervorst W, Temst K and Vantomme A 2012 *J. Phys. D: Appl. Phys.* **45** 405004

[38] Felcher G P, Hilleke R O, Crawford R K, Haumann J, Kleb R and Ostrowski G 1987 *Rev. Sci. Instrum.* **58** 609

[39] Demeter J, Teichert A, Kiefer K, Wallacher D, Ryll H, Menéndez E, Paramanik D, Steitz R, Van Haesendonck C, Vantomme A and Temst K 2011 *Rev. Sci. Instrum.* **82** 033902

[40] Demeter J, Menéndez E, Teichert A, Steitz R, Paramanik D, Van Haesendonck C, Vantomme A and Temst K 2012 *Solid State Commun.* **152** 292

[41] Mezei F, Golub R, Klose F and Toews H 1995 *Physica B* **213–214** 898

[42] http://icsd.fiz-karlsruhe.de/icsd/. Access date: 29/10/2013

[43] Harres A and Geshev J 2012 *J. Phys.: Condens. Matter* **24** 326004

[44] Gredig T, Krivorotov I N and Dan Dahlberg E 2006 *Phys. Rev. B* **74** 094431

[45] Gredig T, Krivorotov I N and Dan Dahlberg E 2002 *J. Appl. Phys.* **91** 7760

[46] Radu F, Etzkorn M, Siebrecht R, Schmitte T, Westerholt K and Zabel H 2003 *Phys. Rev. B* **67** 134409